

Internal and near-wall flow fields around a structured porous coated cylinder and their role in passive flow and noise control

Arcondoulis, Elias J. G.; Liu, Yu; Yang, Yannian; Ragni, D.; Rubio Carpio, A.; Avallone, F.

DOI

[10.2514/6.2021-2226](https://doi.org/10.2514/6.2021-2226)

Publication date

2021

Document Version

Final published version

Published in

AIAA AVIATION 2021 FORUM

Citation (APA)

Arcondoulis, E. J. G., Liu, Y., Yang, Y., Ragni, D., Rubio Carpio, A., & Avallone, F. (2021). Internal and near-wall flow fields around a structured porous coated cylinder and their role in passive flow and noise control. In *AIAA AVIATION 2021 FORUM* Article AIAA 2021-2226 (AIAA Aviation and Aeronautics Forum and Exposition, AIAA AVIATION Forum 2021). <https://doi.org/10.2514/6.2021-2226>

Important note

To cite this publication, please use the final published version (if applicable).
Please check the document version above.

Copyright

Other than for strictly personal use, it is not permitted to download, forward or distribute the text or part of it, without the consent of the author(s) and/or copyright holder(s), unless the work is under an open content license such as Creative Commons.

Takedown policy

Please contact us and provide details if you believe this document breaches copyrights.
We will remove access to the work immediately and investigate your claim.



Internal and near-wall flow fields around a structured porous coated cylinder and their role in passive flow and noise control

Elias J. G. Arcondoulis*, Yu Liu[†] and Yannian Yang[‡]

Southern University of Science and Technology, Shenzhen, Guangdong Province, 518055, P. R. China

Daniele Ragni[§], Alejandro Rubio Carpio[¶] and Francesco Avallone^{||}

Delft University of Technology, Delft 2629HS, The Netherlands

The mechanisms responsible for vortex shedding reduction, due to the application of a porous coating to a smooth cylinder placed in uniform flow, are still uncertain despite several numerical and experimental studies. To help understand these mechanisms, a transparent Structured Porous Coated Cylinder (SPCC) was manufactured to investigate the internal and near-wall flow fields. The SPCC mimics the more commonly used porous materials such as metal foam and polyurethane, that possess randomized structures preventing a clear line-of-sight along the span and circumference of the porous layers. Tomographic Particle Image Velocimetry was used in a water-tunnel facility to investigate three small regions of an SPCC, on the windward, mid-region and leeward sides. In this paper, previously unseen experimentally obtained internal flow fields of a porous coated cylinder are presented. The following summarize the key observations (1) stagnation from freestream flow to the inner cylinder diameter in the windward region, (2) boundary layer profiles within the porous layer in the circumferential mid-region and (3) bleeding from the porous layer into the wake in the leeward region. These results provide key experimental findings for comparison and validation of numerical simulations of bulk porous media, such as the Darcy-Forscheimer method used in conjunction with the Ffowcs Williams-Hawkings acoustic analogy.

Nomenclature

d	=	bare cylinder diameter (mm)
D	=	porous coated cylinder outer diameter (mm)
f	=	acoustic frequency (Hz)
r	=	radial distance from the bare cylinder diameter (mm)
Re	=	Reynolds number
St	=	Strouhal number
t	=	porous coating thickness (mm)
\overline{U}	=	time-averaged velocity (m/s)
U_0	=	freestream flow velocity (m/s)
$\overline{u}, \overline{v}, \overline{w}$	=	time-averaged velocity components in the x -, y - and z -directions (m/s)
u', v'	=	fluctuating velocity components in the x - and y -directions (m/s)
x, y, z	=	local coordinate directions
α	=	angle between the camera lens and the laser sheet ($^\circ$)
δ	=	boundary layer thickness (mm)
θ	=	cylinder circumferential angle ($^\circ$)
ϕ	=	porosity (%)

*Research Assistant Professor, Department of Mechanics and Aerospace Engineering, Senior AIAA Member

[†]Associate Professor, Department of Mechanics and Aerospace Engineering, Senior AIAA Member

[‡]Research Assistant Professor, Department of Mechanics and Aerospace Engineering, AIAA Member

[§]Associate Professor, Department of Aerodynamics, Wind Energy, Flight Performance & Propulsion, AIAA Member

[¶]PhD Candidate, Department of Aerodynamics, Wind Energy, Flight Performance & Propulsion, Student AIAA Member

^{||}Assistant Professor, Department of Aerodynamics, Wind Energy, Flight Performance & Propulsion, AIAA Member

I. Introduction

THE application of passive flow control techniques for cylindrical bodies has grown in importance for several commercial and industrial applications. Some examples include sections of high speed train pantographs [1], aircraft landing gear [2] and electrical power lines. Numerical studies of a Porous Coated Cylinder (PCC) have been shown to cause a reduction of tonal noise amplitude and decrease the tone frequency [3–5]. Geyer and Sarradj [6] observed that by applying a porous coating to a cylinder can also decrease much of the broadband noise, in agreement with their following numerical simulations [7]. An interesting observation is that Sueki et al. [1] experimentally showed that the material type (i.e., comparing a Metal Foam Porous Coated Cylinder (MFPCC) to a Polyurethane Porous Coated Cylinder (PPCC)) had little or no impact on the measured noise reduction. This important study revealed that the porous material thickness, porosity and spacings of the pores were of greatest importance in tonal and broadband noise reduction. Furthermore, suitable application of a porous coating to the cylinder leeward surface can lead to a significant reduction of drag as compared to a bare cylinder [8].

The important properties of porous media include the numbers of Pores Per Inch (PPI) [1, 9] and the porosity, ϕ , as a percentage of the porous media volume with respect to a solid equivalent [4, 5, 10]. The typical experimentally investigated PPI range, using an MFPCC and PPCC for porous coated cylinders is from 10 PPI to 30 PPI [1, 9, 11, 12], with significant vortex shedding tone reduction observed using 10 PPI materials [11, 12]. Arcondoulis et al. [10] designed a Structured Porous Coated Cylinder (SPCC) that has a clear line of sight along the cylinder span, and also from the outer SPCC surface into the internal solid cylinder thus allowing the use of tomographic PIV to obtain some insight on the internal flow fields within the porous layers [13]. They showed that the tone suppression and frequency shift were very similar to PPCCs and MFPCCs with similar porosity and PPI. Figure 1 represents the typical vortex shedding tone reduction of an SPCC [14]. The acoustic spectra clearly shows that the vortex shedding tone exhibited by the bare cylinder is reduced by using an SPCC yet some high-frequency contribution is also observed at frequencies greater than 2000 Hz and a secondary tone at twice the vortex shedding frequency is also observed. While this is not desirable, it is of secondary importance relative to the study of the reduction of the fundamental bare cylinder vortex shedding flow mechanisms.

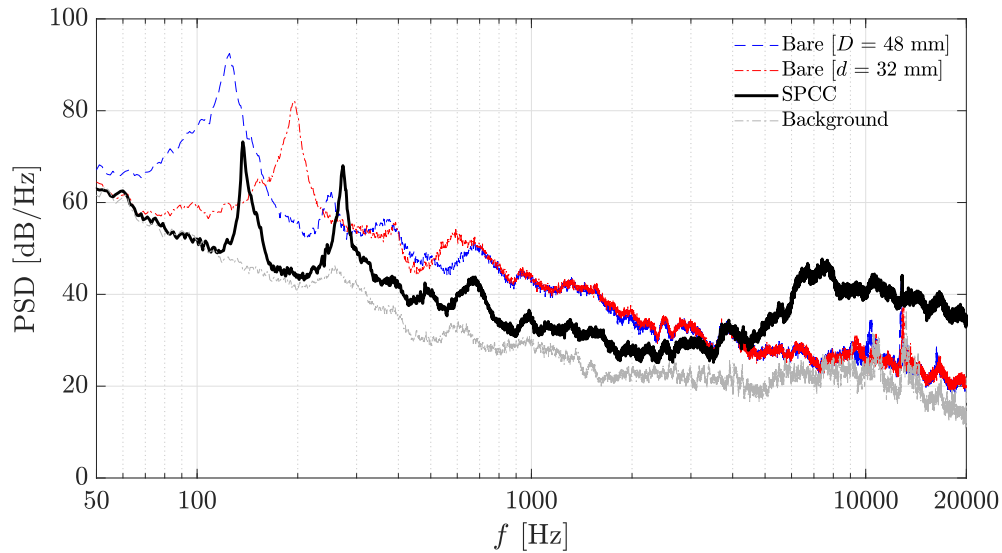


Fig. 1 SPCC and bare cylinder acoustic spectra recorded at $Re = 1.1 \times 10^5$, adapted from Arcondoulis et al. [14].

It is hypothesized that the internal and near-wall flow fields of SPCC should be similar to those of the MFPCC or PPCC, due to their similar acoustic behavior when placed in uniform flow [10]. The near-wall flow field is relatively simple to compare for different cylinder types; the internal flow field and its interaction with the outside one, however, is not as simple to measure and therefore difficult to compare. The internal flow within the randomized porous medium would be extremely difficult to measure without modifying the porous structure and it is therefore likely that these difficulties have led to few publications regarding fundamental fluid mechanics of the internal flow field of a PCC. Via

numerical simulations, Naito and Fukagata [15] proposed that the slip velocity of a PCC can modify the shear layer such that it is less prone to roll up into vortices. Furthermore, they also presented boundary layer profiles of PCCs using a Darcy-Forcheimer porous medium approximation which has not been experimentally verified for the internal flow within the porous layers. Furthermore, they also proposed that the energy of the entrained fluid within the porous layer is dissipated and the ejected low-energy fluid from the PCC leeward side raises the back pressure [15]. At low-Reynolds numbers, Xu et al. [16] conducted a 3-D numerical investigation of flow through a single open cell metal foam pore. This revealed the internal flow field within a single pore yet it is difficult to relate this result to a cylindrical geometry as compared to a single, isolated pore. Despite these numerical simulations, there are no experimental data to verify these results. Zhang et al. [5] and Li et al. [4] used a Darcy-Forcheimer model [17] to investigate the effect of PPI and porosity on the acoustic sound field of PCCs and presented internal boundary layer profiles for each PCC.

In this paper, the SPCC presented by Arcondoulis et al. [10, 18] is tested in a water tunnel using tomographic Particle Image Velocimetry (PIV). By manufacturing the SPCC using a transparent solid material, regions of the internal flow field near the outer diameter was visualized and quantified. Three Fields of View (FOVs) placed at the windward, mid-section and leeward regions of the SPCC were investigated to determine velocity components, vorticity and turbulent kinetic energy. The results obtained from each FOV are discussed separately and related back to numerical and previous experimental results.

II. Cylinder Model

The diameter of the SPCC used for this experimental investigation is larger than those used previously for aeroacoustic and PIV tests in air [10]. This is due to the differences in fluid medium and required pore size to allow a sufficient number of water-borne PIV seeding particles to enter the porous medium. In addition, the maximum allowable cylinder diameter is restricted by the blockage of the cylinder in the water tunnel with a channel height of 300 mm. Furthermore, the minimum allowable cylinder diameter is limited by the capability of manufacturing methods to create a structured porous structure on a smaller scale, where the struts between the pores may be as thin as 1 mm. Therefore, the outer diameter was selected as $D = 96$ mm with an inner bare diameter of $d = 64$ mm and thus the ratio of the porous coating thickness to the bare cylinder diameter, t/d , is 0.25. This t/d ratio is consistent with the aeroacoustic investigation presented in Arcondoulis et al. [10, 18] and within the typical t/d range of others [1, 3, 6, 9, 11, 15, 19, 20]. The SPCC has a span of 385 mm.

It is also important to ensure that the Reynolds number range is within the range of previously published data for comparative purposes. By using $D = 96$ mm and a freestream velocity of $U_0 = 0.8$ m/s, the Reynolds number based on the outer diameter is calculated as $Re = 7.3 \times 10^4$ at a water temperature of 18°C. This Reynolds number is comparable with the published data of both porous coated cylinders [3, 6, 9, 12, 15] and bare cylinders [21–24]. The porosity value, ϕ (%), of the SPCC is identical to previous studies [10, 18], being 87%. A CAD representation of the SPCC is presented in Fig. 2. This geometry was 3-D printed in one-piece using a transparent ultraviolet curing epoxy resin.

The Strouhal number, St , was used to determine the expected shedding frequency of the SPCCs. Based on the calculated Reynolds number range, the porous cylinders are expected to exhibit an approximate Strouhal number of 0.19 [21]; this value is used solely for estimating the shedding tone frequencies. This is consistent with the Strouhal number recorded using a scaled SPCC with identical proportions in a wind tunnel [18], being $St = 0.2$. The relationship between Strouhal number and the vortex shedding frequency (Hz) is provided by $f = StU_0/D$. Based on the values used in this study, the expected vortex shedding frequency is $f = 1.6$ to 1.7 Hz.

III. Experimental Methods

Experiments were conducted in a water tunnel in the Department of Civil Engineering and Geosciences at TU Delft, The Netherlands. This experimental method is identical to a previous investigation [13]. Tomographic PIV was used to record both the internal and near-wall flow field of the SPCC. The low-speed water tunnel has a working section of 400 mm wide and an open channel height of 500 mm. In these experiments, the maximum working height was approximately 300 mm as the maximum water tunnel height should not be reached due to safety purposes. The tunnel is inclined downward at 5° to reduce the required pressure to achieve a specified volumetric flow rate. A pressure-pump is used to control the freestream velocity.

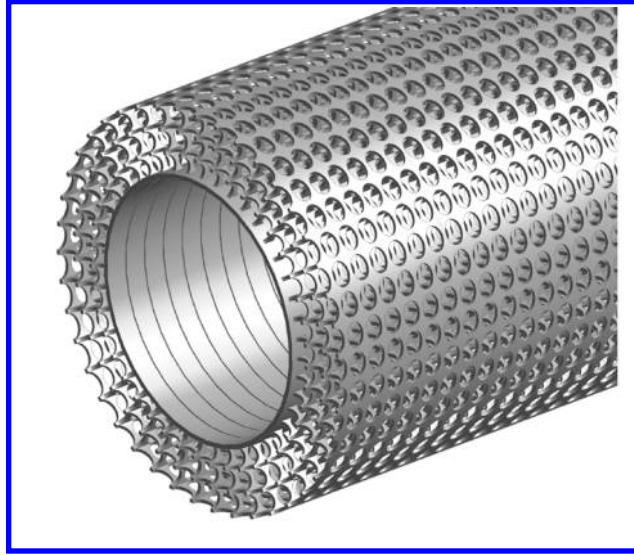


Fig. 2 CAD representation of the SPCC used for tomographic PIV experiments.

A. PIV set-up

The water in the tunnel was seeded with fine silt particles of mean diameter of $100\ \mu\text{m}$ and illumination was provided by a Quantel EverGreen200 Double-Pulse Nd:YAG laser (532 nm wavelength, 200 mJ per pulse). One spherical and two-to-three cylindrical lenses were aligned to produce a 20 mm thick laser sheet. Four LaVision Imagers LX 16M (16MPx, $7.4\ \mu\text{m}$ pixel pitch) were equipped with 105 mm Nikon Micro-Nikkor prime lenses and Scheimpflug adapters were used to align the focal plane with the laser sheet (perpendicular to the water tunnel glass walls). Synchronization of the laser pulses and image acquisition was accomplished using a LaVision programmable timing unit in combination with the LaVision DaVis 8.4 software package. Table 1 summarizes the relevant PIV parameters.

Table 1 Summary of PIV parameters.

Frame type	Double-Frame
Lens focal length	105 mm
Focal ratio ($f/\#$)	16
Field of view (FOV)	(see Fig. 6)
Acquisition frequency (f_{aq})	15 Hz
Pulse separation (Δt)	$600\ \mu\text{s}$
Number of samples (N)	1000
No. images for time-averaging	500

The mirror that reflected the laser sheet into the water was oriented such that a portion of the porous coated media and the cylinder wake were illuminated, as shown in Figs. 4(b) and 3(a). Four-cameras were aligned toward the spanwise centerline of the SPCCs to create an FOV, as depicted in Fig. 3(b) and shown in 4(a). Note that the identified FOV in Fig. 3 is only one of the three FOVs investigated, as discussed in Section B and depicted in Fig. 6.

Calibration of the field of view and self-calibration for the alignment of the imaged volume with the illuminated one was conducted using a Type-7 calibration plate. This plate was placed in contact with the cylinder surface (for a frame of reference) to represent a portion of the FOV. The tunnel was filled with water (at zero velocity) to ensure that any refraction effects between water and air were factored into the calibration. Images were acquired with a calibration plate placed at three spanwise planes with the same xy -coordinates in the spanwise-center of the laser sheet and at the laser sheet edges (i.e., $z = -10\ \text{mm}$, $0\ \text{mm}$ and $10\ \text{mm}$). The LaVision DaVis 8.4 software package was used to complete the calibration stages. The standard MART algorithm with 10 iterations was carried out for the volume reconstruction. Image correlation was carried out with a multi-pass algorithm with a final FOV size (see Fig. 6) and 75% overlap.

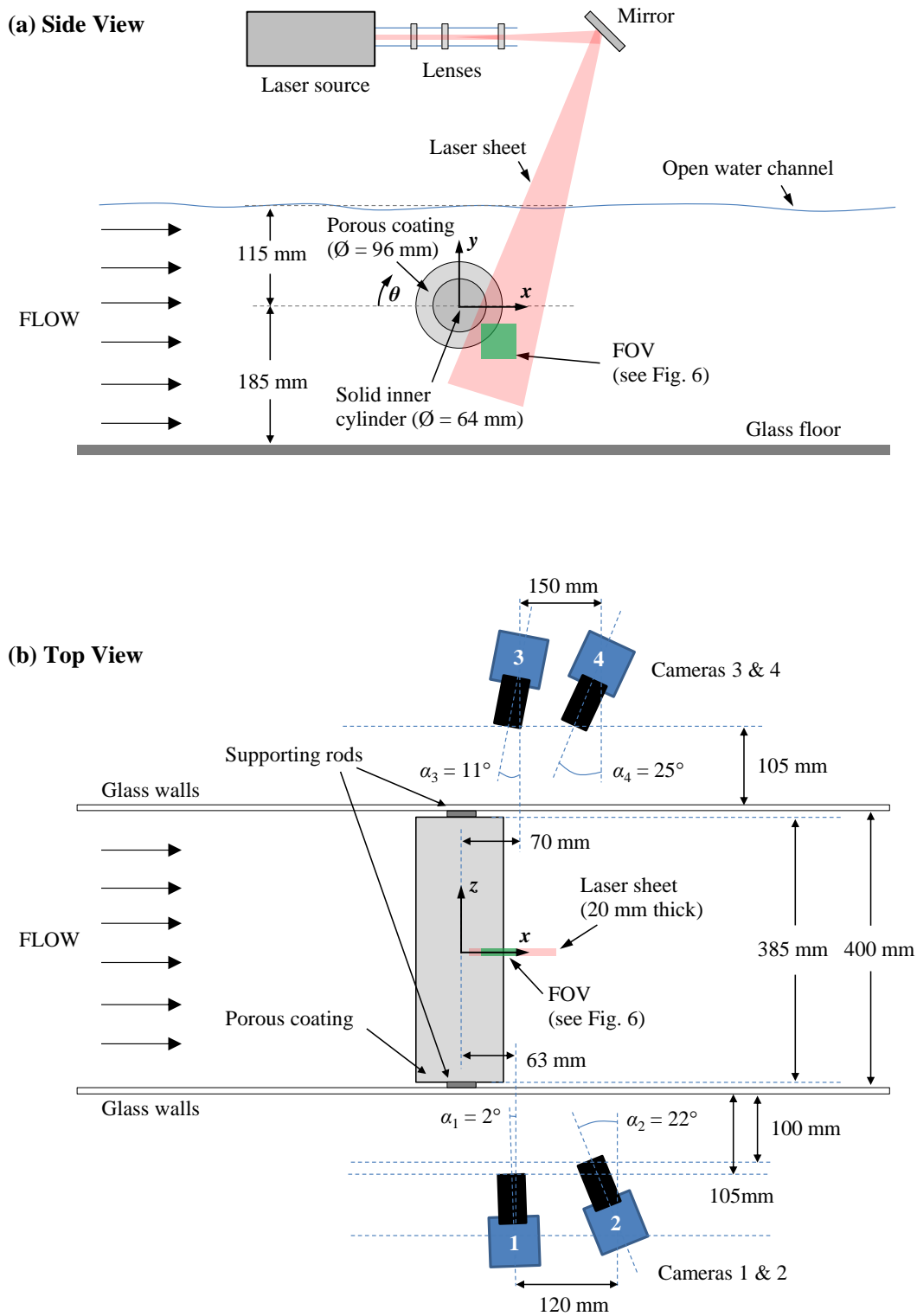


Fig. 3 Schematic diagram of the tomographic PIV configuration (a) Side view and (b) Top View. Images are adapted from Arcondoulis et al. [13] for the same experimental set-up.

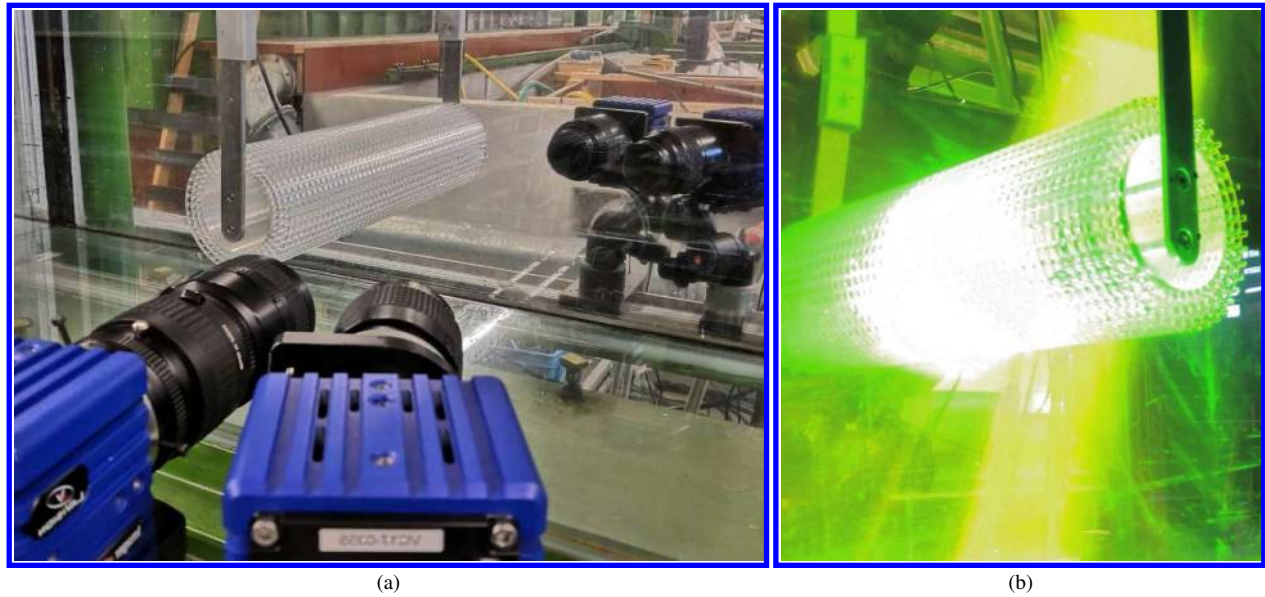


Fig. 4 (a) Photo of the tomographic PIV set-up, showing the cameras aligned toward the SPCC, corresponding to the camera angles in Fig. 3 and (b) Laser light illuminating the rear of the SPCC and the near-wall region for tomographic PIV as depicted in Fig. 3. Photos adapted from Arcondoulis et al. [13].

B. FOV Selection

A flow visualization test was conducted at The University of Adelaide [14] to provide a qualitative understanding of the internal and near-wall flow fields of the SPCC, albeit at a lower Reynolds number of $Re \approx 7000$. A key figure from this study is adapted and presented in Fig. 5. Added to this figure are three rectangular areas of interest, that correspond to the FOVs that are investigated in this study.

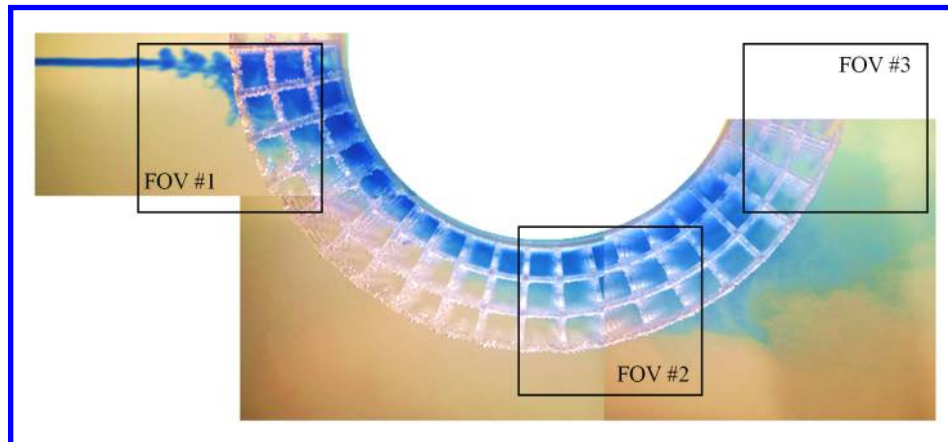


Fig. 5 Three FOV locations used to record critical flow features of the SPCC via tomographic PIV. The flow visualization image is adapted from Arcondoulis et al. [14].

Based on the flow visualization result, the tomographic PIV experiments in FOV #1 will reveal interaction between the freestream flow and the first contact with the porous layer, and how the porous layers affect the stagnation point of the flow and how the flow attaches to the SPCC inner and outer diameters. FOV #2 is likely to reveal the growth and development of the internal and near-wall boundary layer development leading to the rapid development of the wake region. And finally, it can be seen that FOV #3 is within the wake region, in which some recirculation may be observed and some bleeding out of the flow from the porous layer into the wake region. Figure 6 presents the specific locations of

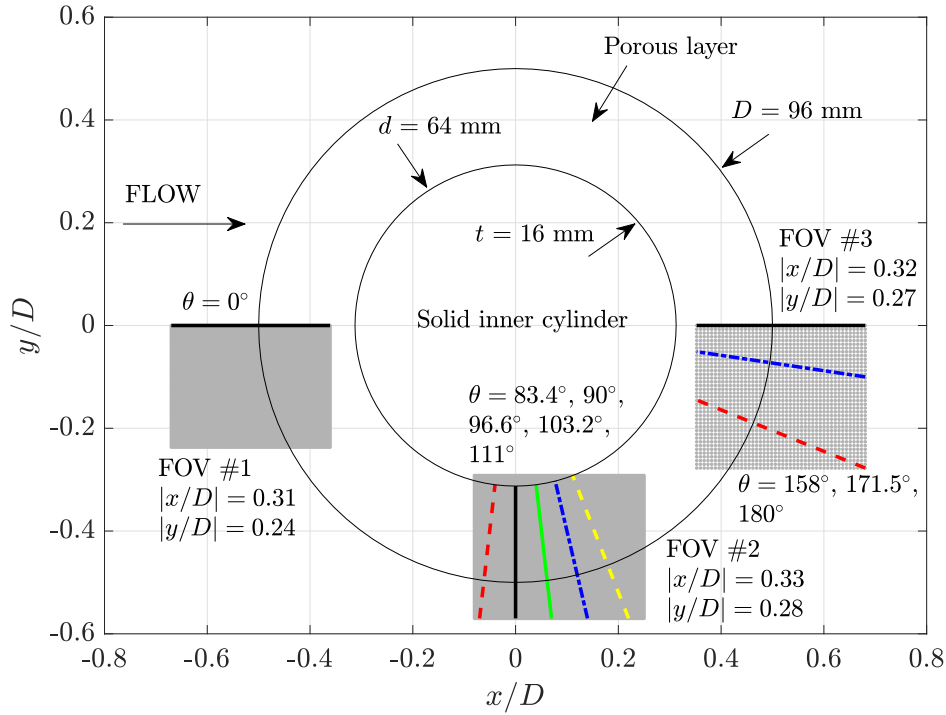


Fig. 6 FOV locations, #1, #2 and #3, used to record critical flow features of the SPCC via tomographic PIV. Lines in each FOV are referred to as θ -lines used during post-processing. Image is to scale.

each FOV.

The dimensions of each FOV vary slightly in the x - and y -directions, due to some FOV cropping during post-processing, where in some cases velocity data on the edges of the FOV were unusable. Note that due to the thickness of the laser sheet, each FOV is 20 mm thick ($z/D = 0.21$) in the z -direction. In Fig. 6 lines are drawn through each FOV, herein referred to as θ -lines. Each θ -line is drawn from as close to the inner diameter as possible, to the appropriate edge of the FOV. The θ -lines are each attributed a θ -angle along which velocity, turbulent kinetic energy and 2-D vorticity are investigated, in some cases.

Due to some experimental complications, each FOV possesses different resolution. FOV #1 has $93 \times 71 \times 59$, FOV #2 has $115 \times 97 \times 51$ and FOV #3 has $46 \times 39 \times 16$ data points in xyz -space. Of most critical importance in this study, is the flow in FOV #2 that will reveal the internal boundary layer development, that has the highest resolution of any FOV in the xy -plane.

IV. Results

A. Windward Region: FOV #1

Figure 7 presents the time-averaged velocity fields at the near-wall and within the porous layer for FOV #1, averaged in the z -direction. These results were averaged in the z -direction to reduce the total amount of presented results. It is future work to investigate the influence of the spanwise direction of each velocity component. The combined flow field of each velocity component is presented in Fig. 7(a), that illustrates flow acceleration around the cylinder and stagnation near and within the porous layer. The value of U was calculated at each time step via $U = \sqrt{u^2 + v^2 + w^2}$ per z -plane, and then averaged over the z -planes. Within the porous layer $\bar{U}/U_0 \neq 0$ and small regions of $\bar{U}/U_0 = 0$ are identified near the SPCC outer diameter. The small regions of stagnation correspond to the locations of the structural members of the SPCC, and between these small stagnation regions are the open pores of the SPCC. Note that at the location of these structural members $\bar{U}/U_0 \neq 0$, which is due to the averaging of velocities over the z -planes, where in some instances

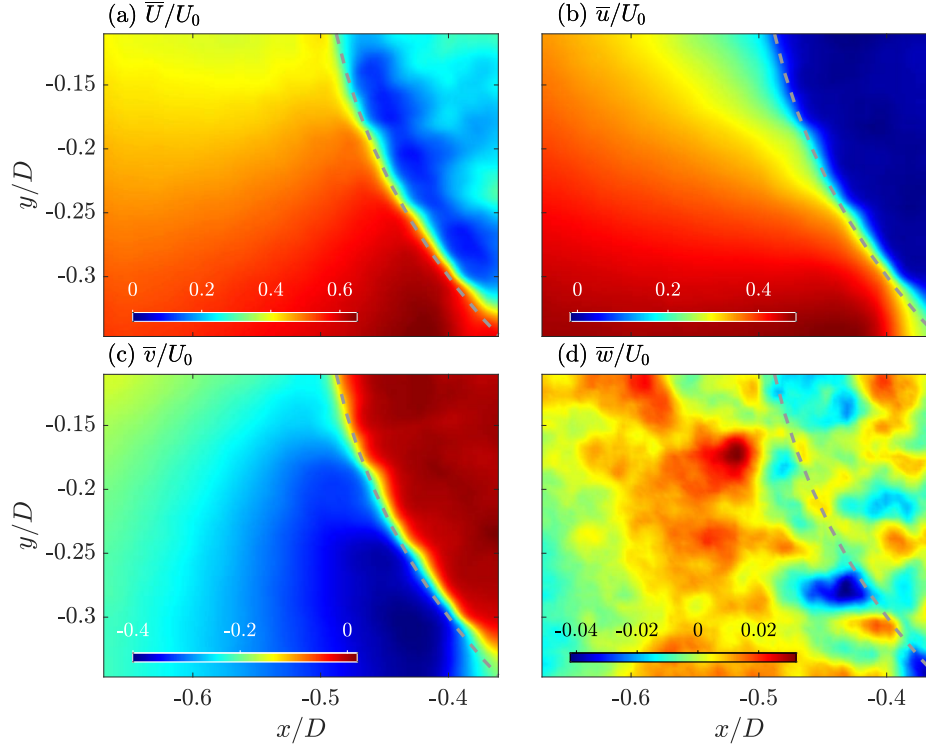


Fig. 7 Time-averaged velocity components recorded in FOV #1 averaged over all z -planes. A dotted line is drawn to denote the outer diameter of the SPCC. Flow is from left to right. (a) \bar{U}/U_0 , (b) \bar{u}/U_0 , (c) \bar{v}/U_0 and (d) \bar{w}/U_0 .

there are open pores. By observation of each flow component, the $\bar{U}/U_0 \approx 0.25$ to 0.3 region is explained by the flow attempting to flow around porous structures which is highly 3-D in nature, in that the flow around a pore will be highly vortical and chaotic and vary per z -plane.

To further understand the flow field, consider the time-averaged x -component of velocity, \bar{u}/U_0 , presented in Fig. 7(b). The flow decelerates in the x -direction upon entering the porous layer, revealing a large stagnation zone. To further investigate how the freestream flow penetrates the porous layer, values of \bar{u}/U_0 were recorded along a horizontal line at $\theta = 0^\circ$ in FOV #1 as identified in Fig. 6. These results are presented in Fig. 8. The presented data are plotted on an r/t -axis, where \bar{u}/U_0 is plotted on a radial axis normalized by the porous layer thickness, t . The value $r/t = 0$ denotes the inner cylinder diameter, d (corresponding to $x/D = -0.3125$) and $r/t = 1$ represents the outer diameter, D (i.e., $r/t = 1$ is at $x/D = -0.5$). This plot clearly shows the gradual flow deceleration towards the outer porous layer and the rapid deceleration once the flow enters the porous layer. Within a range of $0.2t$ from the outer diameter toward the center, the flow decelerates from $\bar{u}/U_0 = 0.2$ to 0 . From $r/t = 0$ to 0.8 , the time-averaged flow field is significantly less along $\theta = 0^\circ$ with some weak reverse flow regions.

By also considering the time-averaged y -component of velocity, \bar{v}/U_0 , in Fig. 7(c), the combined flow field of positive x -direction and negative y -direction reveals that the flow is traveling around the cylinder, consistent with any smooth cylinder body. A local flow acceleration region is observed in both the x - and y -components of velocity in the region of $x/D = -0.5$ to -0.4 and $y/D = -0.35$ to -0.25 , which is also consistent with flows around smooth cylindrical bodies. The flow can be seen to develop around the cylinder and a boundary layer can be observed very close to the wall. The out-of-plane velocity in the z -direction, \bar{w}/U_0 , is presented in Fig. 7(d). Within the porous layer, the flow can be seen to stagnate at porous structural members and also flow between and around them. At the near-wall region, flow in the negative z -direction is seen close to the cylinder, and flow in the positive z -direction is seen away from the cylinder. This shows that there is some spanwise flow behavior internally and at the near-wall region.

The normalized time-averaged z -component of vorticity, $|\omega_z|D/U_0$, calculated at various z -planes is presented in Fig. 9. The local maxima in vorticity may be interpreted as small highly rotational regions as the flow attempts to enter the porous structure around a porous structural member, in conjunction with the shear flow around the outer diameter.

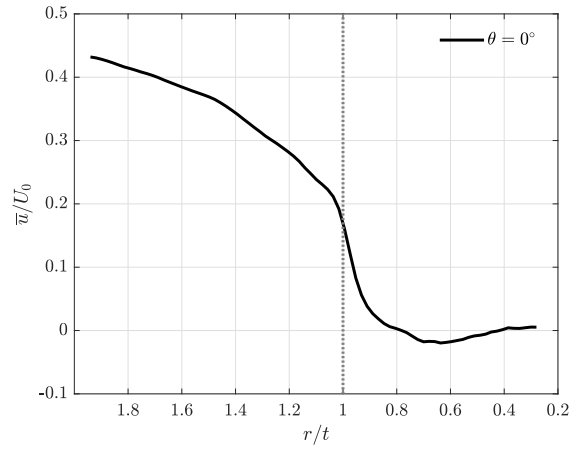


Fig. 8 Time-averaged x -component of velocity, \bar{u}/U_0 , recorded along the FOV #1 θ -line. A vertical dotted line is drawn at $r/t = 1$ to denote the outer diameter of the SPCC. Flow is from left to right.

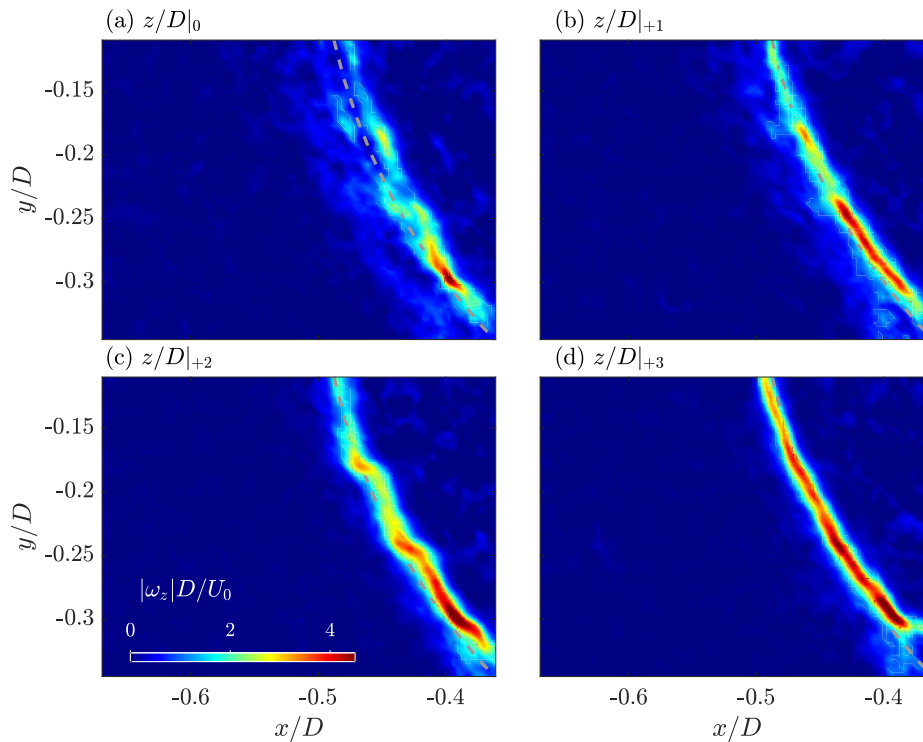


Fig. 9 Normalized z -component vorticity, $|\omega_z|D/U_0$, for FOV #1 obtained at various z/D -planes, separated by $z/D = 0.013$. A dotted line is drawn to denote the outer diameter of the SPCC. Flow is from left to right. (a) $z/D|_0$, (b) $z/D|_{+1}$, (c) $z/D|_{+2}$ and (d) $z/D|_{+3}$.

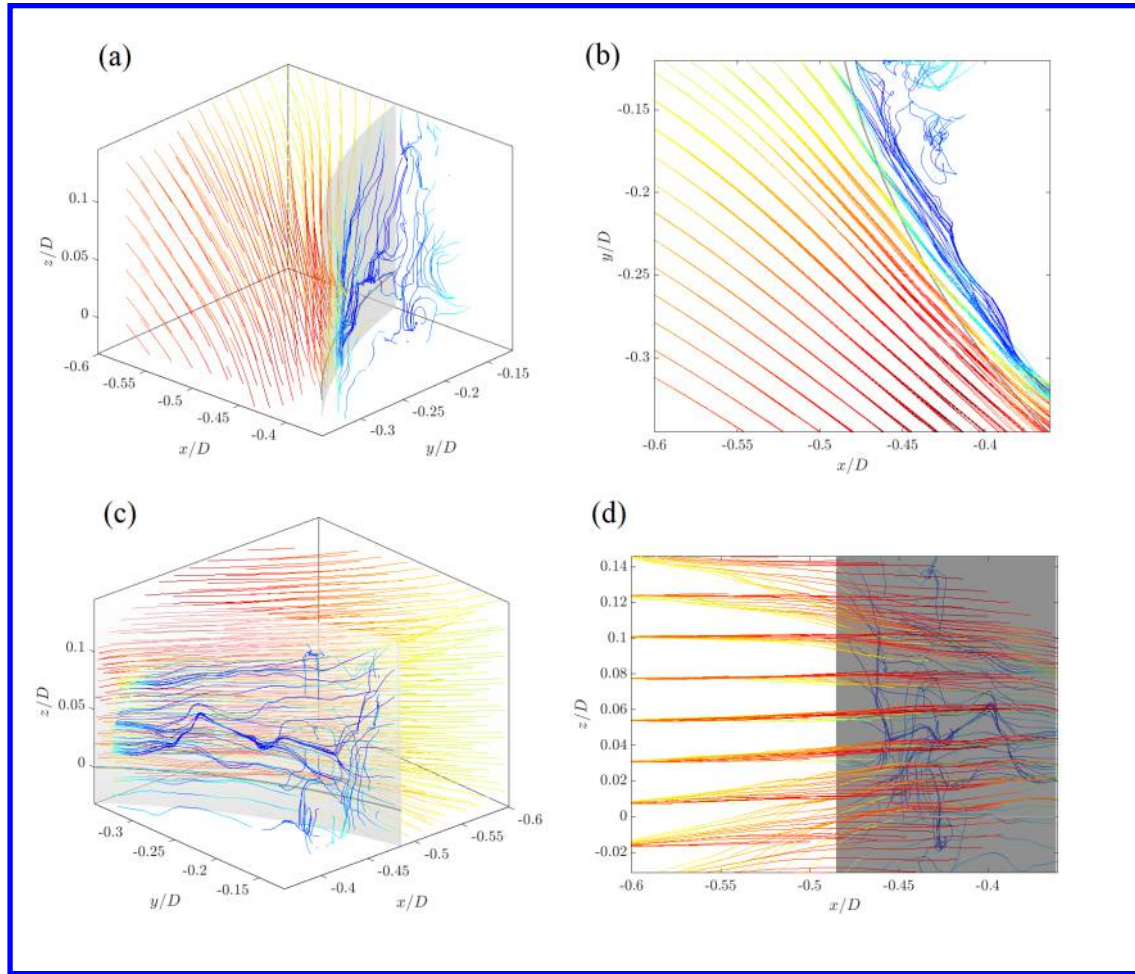


Fig. 10 3-D streamlines of normalized time-averaged velocity within FOV #1. Curves are added to each plot to help visualize the SPCC outer diameter (a) 3-D view, (b) view along the z -axis, (c) image (a) rotated by 180° about the z -axis and (d) view along the y -axis. The color scheme of blue to red is zero to maximum velocity within the presented domain.

This explains why the peak vorticity values are greater at lower y/D -values, as the flow speed is higher there and has a narrower line-of-sight to enter the structure, due to the angle of the porous layer relative to the y -axis, thus leading to a greater intensity of flow rotation about these pores. At different z/D -locations, the location and magnitude of peak vorticity is seen to change, by inspecting Figs. 9(a) through 9(d). At Fig. 9(a) the z/D -plane corresponds to a plane that passes through the center of a pore, and in $z/D = 0.013$ increments, the planes of Figs. 9(b) through 9(d) shift in the z -direction toward a structural member (edge of a pore) that restricts incoming flow. This explains why at a particular z/D -plane, the flow is observed to enter a pore without obstruction ($z/D|_0$) yet at the same x/D and y/D location but with a different z/D -plane, this point corresponds to a porous structural member ($z/D|_{+3}$), and hence a significant increase in the z -component of vorticity is observed.

To further visualize the velocity field in FOV #1, 3-D streamlines of \bar{U}/U_0 are presented in Fig. 10. By looking at Figs. 10(a) and 10(d), it can be seen that there indeed exists variation of the velocity field in the z -direction, as the streamlines appear to bunch toward a small region with increasing x/D . This is an indication of some spanwise variation in the flow field that is likely to have an impact on the spanwise coherence of the SPCC. Note that Fig. 10(b) represents the same view of the flow field as presented in Fig. 7(a). Figure 10(c) is a view from inside the porous layer, looking outward in the negative xy -direction and shows the flow accelerating past the SPCC outer diameter and some of the chaotic flow behavior within the porous layer.

B. Mid-Region: FOV #2

Time-averaged velocity fields at the near-wall and within the porous layer for FOV #2, averaged in the z -direction, are presented in Fig. 11. By observation of Figs. 11(a) and 11(b) that present \bar{U}/U_0 and \bar{u}/U_0 , respectively, closer to the inner cylinder diameter the flow speed is considerably lower than near the SPCC outer diameter. Furthermore, the region of lower flow speed region grows in size with increasing streamwise distance. This reveals that a boundary layer has developed on the inner cylinder diameter within the porous layer. The boundary layer then grows further downstream rapidly and expands out of the porous layer beyond the SPCC outer diameter. By also considering \bar{v}/U_0 in Fig. 11(c), the y -component of velocity also grows similarly to the x -component with both increasing radial and x -distance. A region of spanwise flow, \bar{w}/U_0 , is also observed in Fig. 11(d), within the developed boundary layer region. This is due to the flow slowly spanning laterally in the porous layer at $\theta \approx 90^\circ$, which is in agreement with a flow visualization test of the same SPCC [14].

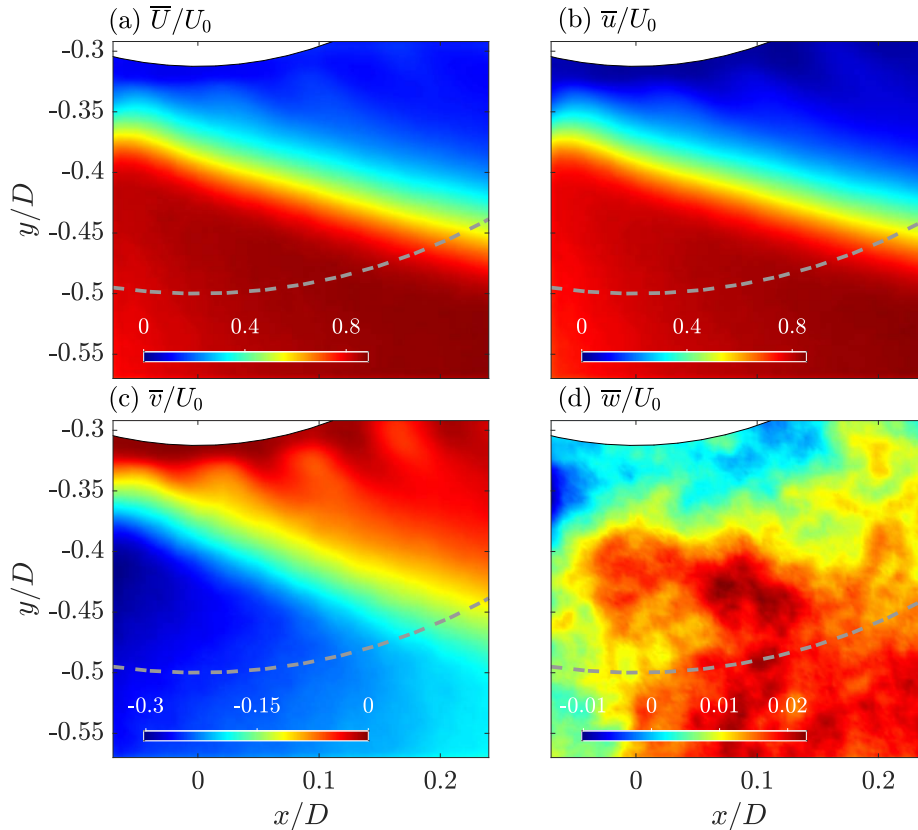


Fig. 11 Time-averaged velocity components recorded in FOV #2 averaged over all z -planes. A dotted line is drawn to denote the outer diameter of the SPCC. Flow is from left to right. (a) \bar{U}/U_0 , (b) \bar{u}/U_0 , (c) \bar{v}/U_0 and (d) \bar{w}/U_0 .

Plots of time-averaged velocity values along lines of investigation (see Fig. 6) within FOV #2 are presented in Fig. 12 to shed more light on the development of the boundary layer within the porous layer and in the near-wall flow region of the SPCC, at $\theta = 83.4^\circ, 90^\circ, 96.6^\circ, 103^\circ$ and 111° . Figure 12(a) presents the boundary layer profiles calculated along each θ -line, in terms of the time-averaged tangential velocity component, \bar{u}_θ/U_0 , plotted against r/t at an arbitrary z -plane (by definition, $\bar{u}_\theta/U_0 = \bar{u}_x/U_0$ at $\theta = 90^\circ$). Note that the boundary layer profiles, for each velocity component considered, showed little spanwise variation and the boundary layer development calculated on each z -plane is indicative of the results in Fig. 12. The boundary layer profile at $\theta = 90^\circ$ is first considered. From the inner diameter, $r/t = 0$, to the outer diameter, $r/t = 1$, the velocity develops from $\bar{u}_\theta/U_0 \approx 0$ to 1. If the boundary layer is considered to develop solely over the inner cylinder diameter (for numerical purposes), then the boundary layer thickness, δ , at $\theta = 90^\circ$ is $\delta|_{90^\circ} = 0.8t = 0.8 \times 0.25d = 0.2d$ (note that $0.2d$ equates to $0.133D$). As expected with developing boundary flows, the boundary layer thickness increases with increasing θ .

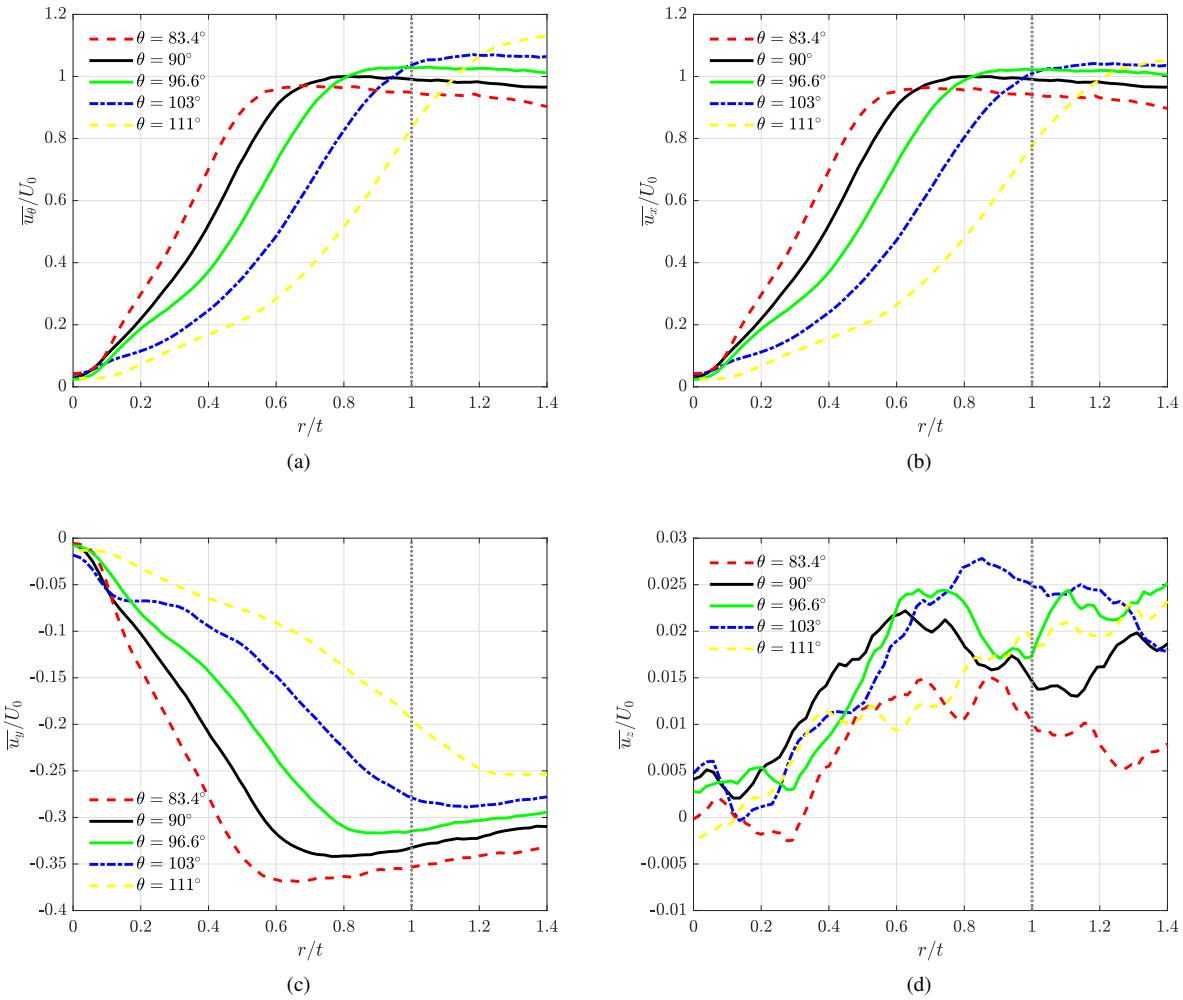


Fig. 12 Boundary layer profiles for various flow components recorded along FOV #2 θ -lines, shown in Fig. 6. A vertical dotted line is drawn at $r/t = 1$ to denote the outer diameter of the SPCC. (a) \bar{u}_θ/U_0 , (b) \bar{u}_x/U_0 , (c) \bar{u}_y/U_0 and (d) \bar{u}_z/U_0 .

To compliment the \bar{u}_θ/U_0 results presented in Fig. 12(a), the \bar{u}_x/U_0 and \bar{u}_y/U_0 values are presented in Figs. 12(b) and (c), respectively. The flow in the x -direction is typically similar to \bar{u}_θ/U_0 ($\bar{u}_\theta/U_0 = \bar{u}_x/U_0$ at $\theta = 90^\circ$, by definition). The y -component of velocity reveals that for each θ -line that the normal flow component from within the porous layer to beyond the SPCC outer diameter increases rapidly from $r/t = 0$. Values of \bar{u}_z/U_0 along the FOV #2 θ -lines are presented in Fig. 12(d). Near the inner diameter, from $r/t = 0$ to 0.4, there is little time-averaged spanwise velocity ($\bar{u}_z/U_0 < 0.01$) yet this velocity increases markedly typically from $r/t = 0.4$ to 0.6. This reveals that the lateral flow in the spanwise direction within the porous layer occurs during the boundary layer growth phase, when $\bar{u}_\theta/U_0 \geq 0.5$. At the SPCC outer diameter and $r/t > 1$, there is no clear relationship between each θ -line and \bar{u}_z/U_0 as the flow is clearly chaotic and possessing lateral fluctuations along the SPCC span. To further investigate the vortical nature of the flow within the porous layer in FOV #2, $|\omega_z|D/U_0$ is presented with superimposed streamlines in Fig. 13.

The region of relative high-vorticity values presented in Fig. 13 is consistent with where the boundary layer profiles possess a high slope (i.e., $d\bar{u}_\theta/U_0/dr \gg 0$). The greatest vorticity is observed closest to $\theta = 90^\circ$, where values of $\bar{u}_x/U_0 \approx 1$ within the porous layer, thereby causing interaction with the porous structural members and generating vortices. At larger values of θ , $\bar{u}_x/U_0 \approx 1$ occurs further from the porous layer and therefore does not produce the same vorticity due to the lack of interaction with the porous structure. Along the inner cylinder diameter, an alternating pattern of vorticity can be observed, with $|\omega_z|D/U_0$ values of 0.12, 0.08, 0.06 and 0.04. The regular spacing of these

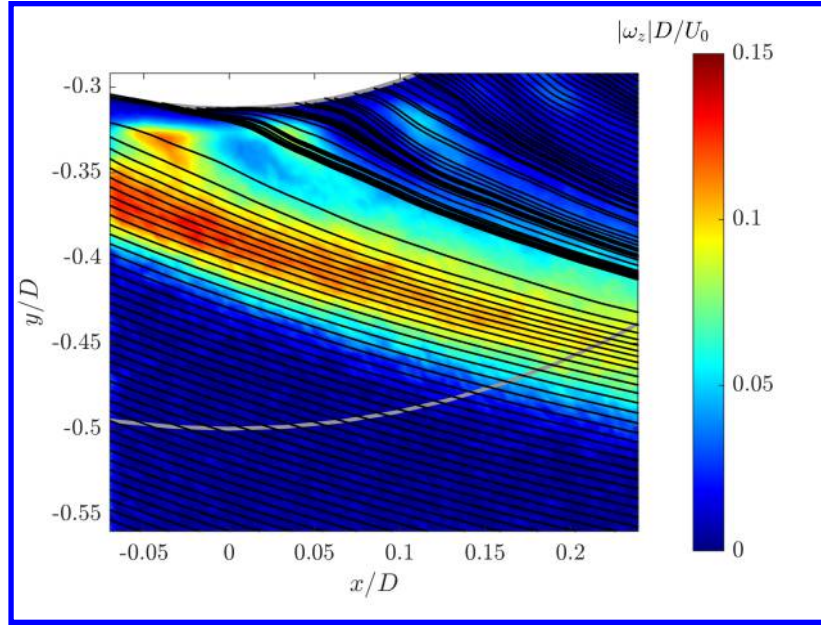


Fig. 13 Normalized 2-D vorticity in the z -plane, $|\omega_z|D/U_0$, and superimposed streamlines, recorded in FOV #2. A dotted line is drawn to denote the outer diameter of the SPCC. Flow is from left to right.

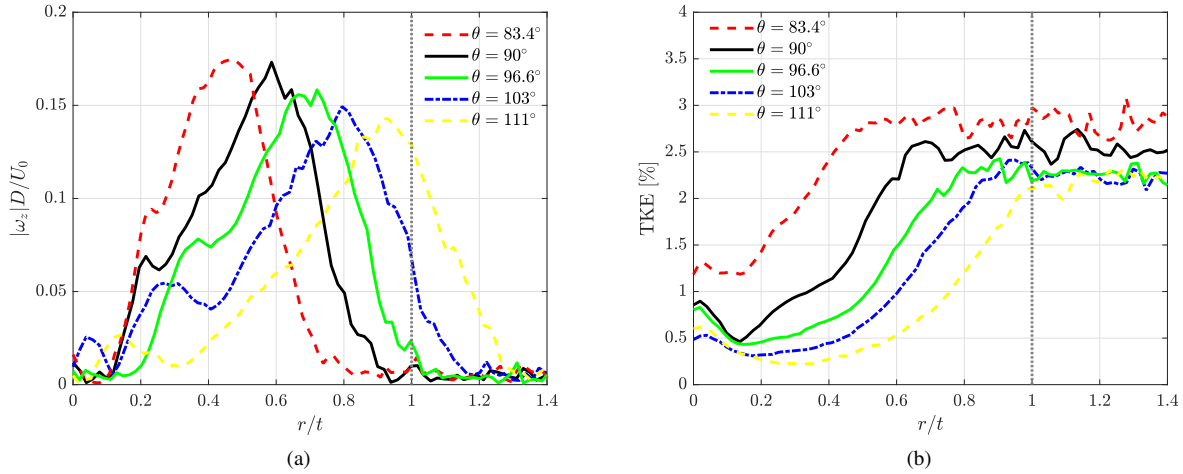


Fig. 14 Normalized 2-D vorticity in the z -plane and 2-D TKE recorded along FOV #2 θ -lines, shown in Fig. 6. A vertical dotted line is drawn at $r/t = 1$ to denote the outer diameter of the SPCC. (a) $|\omega_z|D/U_0$ (b) TKE [%].

small regions of vorticity, in combination with the streamlines in their vicinity, represents the vorticity caused by the normal flow component from the inner cylinder passing around the pore structure.

The 2-D vorticity values in FOV #2 were evaluated along the FOV #2 θ -lines and are presented in Fig. 14(a). These data reveal the distribution of vorticity along a θ -line with respect to normalized distance from the inner diameter, r/t . The width of the vorticity band in terms of r/t is seen to increase with θ -values and also $|\omega_z|_{\max}D/U_0 \propto 1/\theta$. To further investigate the flow behavior in the porous layer and near-wall region, the normalized 2-D turbulent kinetic energy (TKE) [%] was calculated via

$$\text{TKE} = 100 \times \frac{\left(\overline{u'^2} + \overline{v'^2}\right)}{2U_0^2} \quad (1)$$

where u' and v' are the fluctuating x - and y -velocity components, respectively. The TKE is calculated along the FOV #2 θ -lines and is presented in Fig. 14(b). The increase in TKE, relative to r/t , bears a similar profile to the development of the boundary layer. This figure reveals that the peak TKE values occur near the SPCC outer diameter and the near-wall region. The maximum TKE values recorded in the near-wall region for $r/t \geq 1$ are comparable with another SPCC wind tunnel test [14] where at $x/D = 0.75$, $\text{TKE}|_{\max} \approx 3\%$ where TKE was calculated as $100 \times (\overline{u'^2}/U_0^2)$ [%] using hot-wire anemometry.

C. Leeward Region: FOV #3

The time-averaged velocity fields averaged in the z -direction of FOV #3 are presented in Fig. 15. As expected from Fig. 5, the velocity in the wake and near-wall of the leeward SPCC side is expected to be much reduced from the freestream [10, 14, 18]. The flow field results in Fig. 15 verify this and show that much of the flow is entrained within the porous layer. By considering the x -, y - and z -components of velocity, in Figs. 15(b), 15(c) and 15(d), respectively, it can be seen that little of the flow from within the porous layer travels out of the porous layer. The region of relative higher velocity from outside the porous layer is likely to be caused by a 3-D recirculation zone in the near-wake of an SPCC [10] or other PCCs [4, 5].

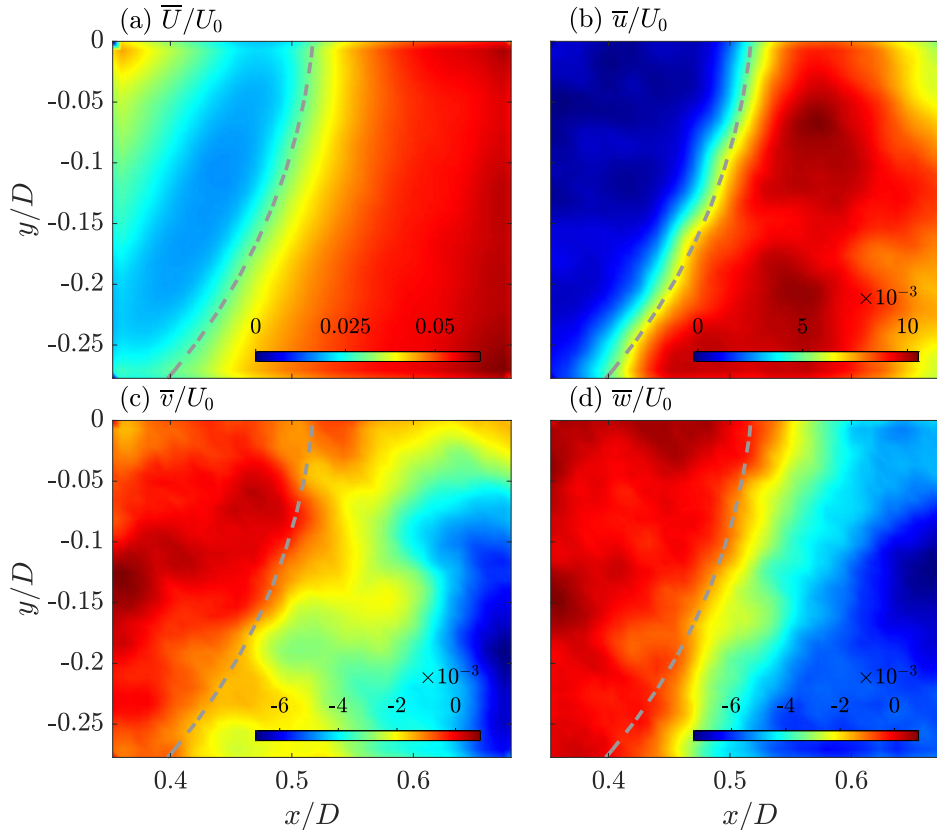


Fig. 15 Time-averaged velocity components recorded in FOV #3 averaged over all z -planes. A dotted line is drawn to denote the outer diameter of the SPCC. Flow is from left to right. (a) \bar{U}/U_0 , (b) \bar{u}/U_0 , (c) \bar{v}/U_0 and (d) \bar{w}/U_0 .

Flow profiles recorded along FOV #3 θ -lines are presented in Fig. 16 to further assist visualizing the transition of flow from internal to external across the SPCC outer diameter. The tangential velocity, \bar{u}_θ/U_0 , in Fig. 16(a) each θ -line reveals a local maxima at $r/t \approx 1.2$ to 1.6 . This is consistent with a recirculation zone in the near-wake of a PCC [4, 5, 10] and that the near-wall flow field near $\theta = 180^\circ$ is not a direct result of bleeding flow from the porous layer into the near-wall region. This is supported by the flow visualization result shown in Fig. 5 [14] that shows bleeding from the porous layer into the near-wall region only from an estimated $\theta \approx 120^\circ$ to 140° . The spanwise

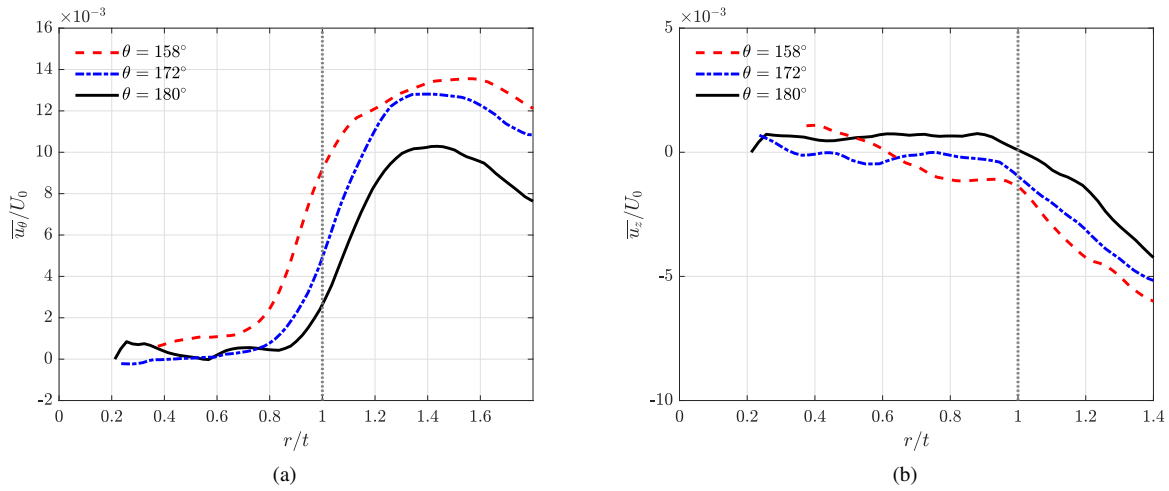


Fig. 16 Internal and near-wall flow profiles recorded along FOV #3 θ -lines, shown in Fig. 6. A vertical dotted line is drawn at $r/t = 1$ to denote the outer diameter of the SPCC. (a) \bar{u}_θ/U_0 and (b) \bar{u}_z/U_0 .

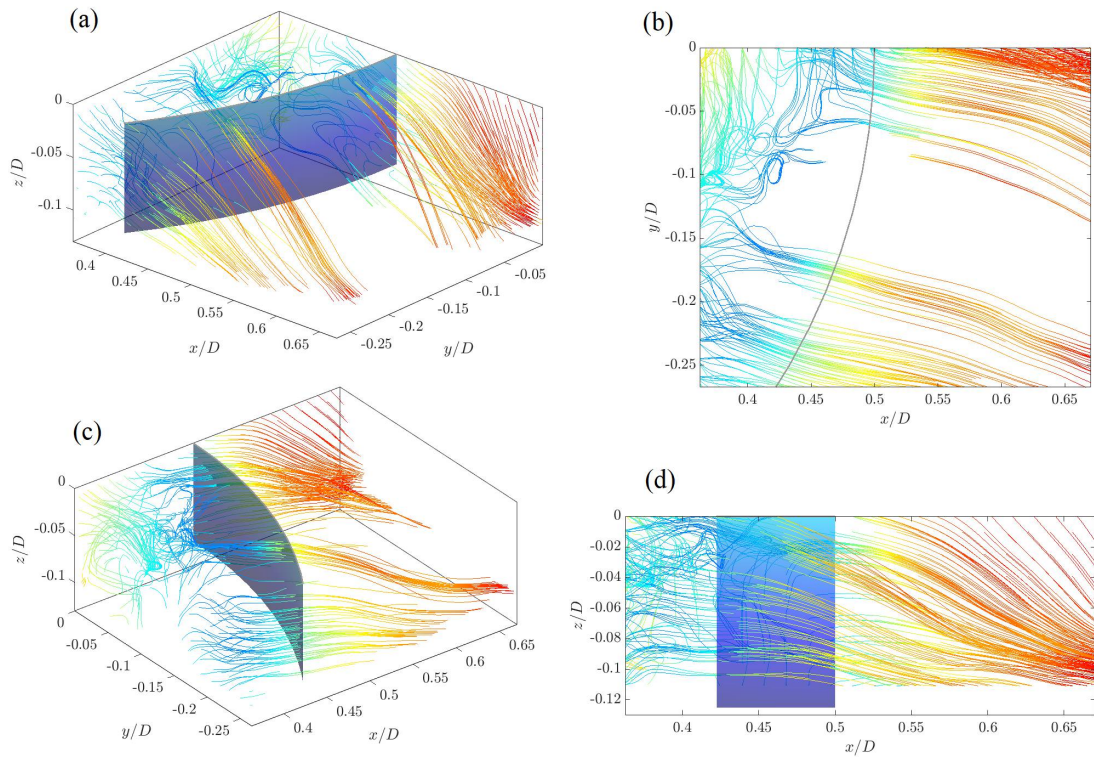


Fig. 17 3-D streamlines of normalized time-averaged velocity within FOV #3. Curves are added to each plot to help visualize the SPCC outer diameter (a) 3-D view, (b) view along the z -axis, (c) image (a) rotated by 180° about the z -axis and (d) view along the y -axis. The color scheme of blue to red is zero to maximum velocity within the presented domain.

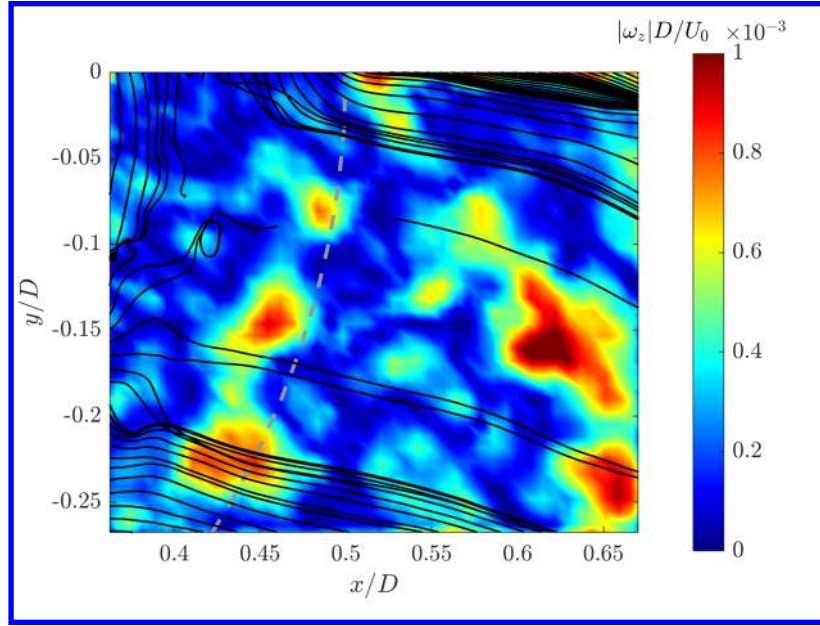


Fig. 18 Normalized 2-D vorticity in the z -plane, $|\omega_z|D/U_0$, and superimposed streamlines, recorded in FOV #3. A dotted line is drawn to denote the outer diameter of the SPCC. Flow is from left to right.

velocity component, $\overline{u_z}/U_0$, in Fig. 16(b) reveals that at $\theta = 180^\circ$ there is negligible spanwise flow velocity within $\overline{u_z}/U_0 = 2 \times 10^{-3}$. With decreasing θ -values small increases in spanwise velocity is observed within the porous layer, due to some weak low-energy vortical structures within the porous layer. At the near-wall region for all θ -values, $\overline{u_z}/U_0 \propto r/t$ and $\overline{u_z}/U_0 \propto \theta$, due to the recirculation zone having a stronger influence on the flow region closer to $\theta = 180^\circ$.

Three-dimensional streamlines within FOV #3 are presented in Fig. 17 to support the explanation of the leeward-side flow mechanisms. In each subfigure, the chaotic flow pattern within the porous layer is evident. Only some small pockets of the internal flow field pass through the SPCC outer diameter. Near $y/D = 0$, the flow is seen to converge in the z -direction to a focal point, which reveals a recirculation zone in the wake. In Fig. 17(b), there is a region from $x/D = 0.45$ to 0.5 and $y/D = -0.08$ to -0.15 of decreased velocity. This represents the transition region between the recirculation zone ($y/D > -0.08$) and some bleeding of the internal flow field into the near-wake region ($y/D < -0.15$). Another region of near-stagnant flow is located at $x/D \approx 0.45$ and $y/D \approx -0.2$. This position coincides with a structural member between pores, hence restricting the flow. These results are supported by the 2-D vorticity plot in the z -plane, $|\omega_z|D/U_0$, as presented in Fig. 18. Along the SPCC outer diameter, there are three distinct small regions of high vorticity that correspond to the pore spacing. By comparing Figs. 17(c) and 18, the vorticity is a result of the two sets of streamlines around the pore structural members. The larger region of vorticity, located at $x/D \approx 0.62$ and $y/D \approx -0.15$ can also be explained by the transition between the recirculation zone and the bleeding of the internal flow that act in opposite directions, thereby generating a localized vortical flow structure.

V. Conclusions

A tomographic PIV investigation of an SPCC was conducted in a water tunnel. Three small regions were investigated, to understand the development of the internal flow fields and the near-wall flow regions, located on the windward, mid-region and leeward sides of the SPCC. The windward FOV revealed localized regions of stagnation within the porous layer that corresponded to the structural members of the SPCC porous layer. Plots of 2-D vorticity revealed the rotational nature of the incoming flow into the porous layer that is forced to rotate about the structural members. The mid-region FOV provided key insight into the development of the internal boundary layer and its development in the circumferential direction. Within the porous layer there exists a noticeable normal flow component away from the SPCC inner diameter that yields localized regions of viscosity, corresponding to flow around porous structural members near the inner diameter. The leeward FOV revealed some bleeding of the entrained flow into the near-wake and also

the presence of a recirculation zone immediately aft of the SPCC. This recirculation zone is 3-D in nature, due to the recorded spanwise velocity in the near-wall region.

The internal and near-wall flow field results presented in this paper are unseen experimentally obtained results. From the conducted experiments, there is still much data to be processed to complete the study and relationship between numerical and experiential results in these critical flow regions of PCCs. Future work will involve processing the time-resolved data, to visualize the development of small-scale vortices that enter and emerge from the porous layer. Key flow field properties, such as the internal boundary layer profile and recirculation zone adjacent to the near-wall in the wake will be compared against numerical studies of PCCs with similar PPI, porosity and Reynolds number.

Acknowledgments

This research was supported by the National Natural Science Foundation of China (Grant No. 11772146). The authors would like to thank Sander de Vree (Department of Civil Engineering and Geosciences, TUDelft) for granting use of the water tunnel and his patience with our experimental procedures and requests, Victor Chavarrias for his assistance in organizing and booking the water tunnel facility and the workshop staff for their assistance and patience during testing. The primary author would also like to acknowledge Pengwei Xu for his assistance in communicating with 3-D printing manufacturers and suppliers.

References

- [1] Sueki, T., Ikeda, M., and Takaishi, T., "Aerodynamic noise reduction using porous materials and their application to high-speed pantographs," *Quarterly Report of RTRI*, Vol. 50, No. 1, 2009, pp. 26–31.
- [2] Boorsma, K., Zhang, X., Molin, N., and Chow, L. C., "Bluff Body Noise Control Using Perforated Fairings," *AIAA Journal*, Vol. 47, No. 1, 2009, pp. 33–43.
- [3] Liu, H., Wei, J., and Qu, Z., "Prediction of aerodynamic noise reduction by using open-cell metal foam," *Journal of Sound and Vibration*, Vol. 331, No. 7, 2012, pp. 1483–1497.
- [4] Li, Z., Tang, T., Liu, Y., Arcondoulis, E. J. G., and Yang, Y., "Numerical study of aerodynamic and aeroacoustic characteristics of flow over porous coated cylinders: Effects of porous properties," *Aerospace Science and Technology*, Vol. 105, 2020, p. 106042.
- [5] Zhang, P., Liu, Y., Li, Z., Liu, H., and Yang, Y., "Numerical study on reducing aerodynamic drag and noise of circular cylinders with non-uniform porous coatings," *Aerospace Science and Technology*, Vol. 107, 2020, p. 106308.
- [6] Geyer, T. F., and Sarradj, E., "Circular cylinders with soft porous cover for flow noise reduction," *Experiments in Fluids*, Vol. 57, No. 3, 2016, p. 30.
- [7] Geyer, T. F., Sharma, S., and Sarradj, E., "Detached Eddy Simulation of the Flow Noise Generation of Cylinders with Porous Cover," *Proceedings of the 2018 AIAA/CEAS Aeroacoustics Conference*, AIAA Paper 2018-3472 (2018).
- [8] Klausmann, K., and Ruck, B., "Drag reduction of circular cylinders by porous coating on the leeward side," *Journal of Fluid Mechanics*, Vol. 813, 2017, pp. 382–411.
- [9] Sueki, T., Takaishi, T., Ikeda, M., and Arai, N., "Application of porous material to reduce aerodynamic sound from bluff bodies," *Fluid dynamics research*, Vol. 42, No. 1, 2010, p. 015004.
- [10] Arcondoulis, E. J. G., Liu, Y., Li, Z., Yang, Y., and Wang, Y., "Structured porous material design for passive flow and noise control of cylinders in uniform flow," *Materials*, Vol. 12, No. 18, 2019, p. 2905.
- [11] Aguiar, J., Yao, H., and Liu, Y., "Passive Flow/Noise Control of a Cylinder Using Metal Foam," *Proceedings of the 23rd International Congress on Sound and Vibration*, 2016, pp. 1–8.
- [12] Ruck, B., Klausmann, K., and Wacker, T., "The flow around circular cylinders partially coated with porous media," *AIP Conference Proceedings*, Vol. 1453, No. 1, 2011, pp. 49–54.
- [13] Arcondoulis, E., Ragni, D., Rubio Carpio, A., Avallone, F., Liu, Y., Yang, Y., and Li, Z., "The internal and external flow fields of a structured porous coated cylinder and implications on flow-induced noise," *Proceedings of the 25th AIAA/CEAS Aeroacoustics Conference*, AIAA Paper 2019-2648 (2019).

- [14] Arcondoulis, E., Liu, Y., Geyer, T. F., Sedaghatzadeh, N., and Arjomandi, M., “Aeroacoustic performance of cylinders with a circumferential varying porous coating,” *AIAA AVIATION 2020 FORUM*, AIAA Paper 2020-2527 (2020).
- [15] Naito, H., and Fukagata, K., “Numerical simulation of flow around a circular cylinder having porous surface,” *Physics of Fluids*, Vol. 24, No. 11, 2012.
- [16] Xu, C., Mao, Y., and Hu, Z., “Numerical study of pore-scale flow and noise of an open cell metal foam,” *Aerospace Science and Technology*, Vol. 82, 2018, pp. 185–198.
- [17] Li, Z., Tang, T., Liu, Y., Arcondoulis, E. J. G., and Yang, Y., “Implementation of compressible porous-fluid coupling method in an aerodynamics and aeroacoustics code—Part II: Turbulent flow,” *Applied Mathematics and Computation*, Vol. 373, 2020, p. 124988.
- [18] Arcondoulis, E. J. G., Geyer, T. F., and Liu, Y., “An investigation of wake flows produced by asymmetrically structured porous coated cylinders,” *Physics of Fluids*, Vol. 33, No. 3, 2021, p. 037124.
- [19] Liu, H., and Azarpeyvand, M., “Passive Control of Tandem Cylinders Flow and Noise Using Porous Coating,” *Proceedings of the 22nd AIAA/CEAS Aeroacoustics Conference*, AIAA Paper 2016-2905 (2016).
- [20] Xia, C., Wei, Z., Yuan, H., Li, Q., and Yang, Z., “POD analysis of the wake behind a circular cylinder coated with porous media,” *Journal of Visualization*, Vol. 21, No. 6, 2018, pp. 965–985.
- [21] Norberg, C., “Fluctuating lift on a circular cylinder: review and new measurements,” *Journal of Fluids and Structures*, Vol. 17, No. 1, 2003, pp. 57–96.
- [22] Jenkins, L., Neuhart, D., McGinley, C., Khorrami, M., and Choudhari, M., “Measurements of unsteady wake interference between tandem cylinders,” *Proceedings of the 36th AIAA Fluid Dynamics Conference and Exhibit*, 2006, p. 3202.
- [23] Neuhart, D., Jenkins, L., Choudhari, M., and Khorrami, M., “Measurements of the flowfield interaction between tandem cylinders,” *Proceedings of the 15th AIAA/CEAS Aeroacoustics Conference*, AIAA Paper 2009-3275 (2009).
- [24] Hutcheson, F. V., Brooks, T. F., Lockard, D. P., Choudhari, M. M., and Stead, D. J., “Acoustics and Surface Pressure Measurements from Tandem Cylinder Configurations,” *Proceedings of the 20th AIAA/CEAS Aeroacoustics Conference*, AIAA Paper 2014-2762 (2014).